remote sensing

MDPI

Article

Sea Fog Detection Based on Normalized Difference Snow Index Using Advanced Himawari Imager Observations

Han-Sol Ryu and Sungwook Hong *

Department of Environment, Energy and Geoinfomatics, Sejong University, Seoul 05006, Korea; hansol@sju.ac.kr
* Correspondence: sesttiya@sejong.ac.kr; Tel.: +82-2-6935-2430

Received: 8 April 2020; Accepted: 8 May 2020; Published: 10 May 2020

check for updates

Abstract: Many previous studies have attempted to distinguish fog from clouds using low-orbit and geostationary satellite observations from visible (VIS) to longwave infrared (LWIR) bands. However, clouds and fog have often been misidentified because of their similar spectral features. Recently, advanced meteorological geostationary satellites with improved spectral, spatial, and temporal resolutions, including Himawari-8/9, GOES-16/17, and GeoKompsat-2A, have become operational. Accordingly, this study presents an improved algorithm for detecting daytime sea fog using one VIS and one near-infrared (NIR) band of the Advanced Himawari Imager (AHI) of the Himawari-8 satellite. We propose a regression-based relationship for sea fog detection using a combination of the Normalized Difference Snow Index (NDSI) and reflectance at the green band of the AHI. Several case studies, including various foggy and cloudy weather conditions in the Yellow Sea for three years (2017–2019), have been performed. The results of our algorithm showed a successful detection of sea fog without any cloud mask information. The pixel-level comparison results with the sea fog detection based on the shortwave infrared (SWIR) band (3.9 μm) and the brightness temperature difference between SWIR and LWIR bands of the AHI showed high statistical scores for probability of detection (POD), post agreement (PAG), critical success index (CSI), and Heidke skill score (HSS). Consequently, the proposed algorithms for daytime sea fog detection can be effective in daytime, particularly twilight, conditions, for many satellites equipped with VIS and NIR bands.

Keywords: sea fog; detection; Himawari; NDSI; algorithm; satellite remote sensing

1. Introduction

Sea fog often causes automobile, aviation, and marine transportation accidents because of its low visibility, with subsequent losses to life and socioeconomic impacts occurring throughout the ocean and in coastal regions [1]. The Yellow Sea, including the Korean western coast and eastern Chinese coast regions, often experiences heavy fog, especially from April to July [2] with the formation of advection cooling fogs [3]. These regions often experience severe fog-related impacts on their seafaring activities. For example, in South Korea, over 50% of 800 sea fog-related ship collisions between 1981 and 2010 occurred in the Yellow Sea due to dense sea fog [4], and a tragic fog-related accident left 11 dead and 50 injured from a pileup of 29 cars and trucks on a major highway near the western coast of South Korea [5].

Fog generally develops at night or during pre-dawn hours [6]. Poor discrimination between fog and clouds has been thoroughly established from many satellite remote sensing studies [7], although it is not difficult for human eyes to identify fog from clouds in visible (VIS) images from satellite observation using different spatial contexts and temporal variations. Cloud mask information has been provided by several satellite sensors, including the Advanced Very-High-Resolution Radiometer

(AVHRR), and Moderate Resolution Imaging Spectroradiometer (MODIS), Visible Infrared Imaging Radiometer Suite (VIIRS) of polar orbiting satellites, Advanced Baseline Imager (ABI), Advanced Meteorological Imager (AMI), and Advanced Himawari Imager (AHI) [8] of geostationary satellites. However, these sensors tend to misidentify fog, sea ice, and snow as clouds because of their similar spectral features in the VIS bands of satellite sensors [9,10]. Notably, the cloud products retrieved at the same bands of different satellites can be quite different because of differing instrument characteristics, spectral response function, physical assumptions, and retrieval algorithm [11,12].

Several fog detection techniques have been developed and utilized based on spectral signatures, radiative properties, and geometrical textures [13–20] during recent decades. The VIS band has been applied to identify sea fog because of the clear contrast in the albedo between foggy and ambient clear areas during the daytime, however, it is limited during night-time owing to the lack of solar irradiation [21]. In the IR band, generally, the difference of brightness temperature between shortwave infrared (SWIR) (3.9 μm) and longwave infrared (LWIR) (10.8 μm) [22], referred to as bispectral image processing (BIP) [23], has been used to distinguish fog from clouds [24]. For example, the negative or near zero values of brightness temperature differences (BTD) between 3.9 and 11 μm channels during the nighttime indicates low stratus/fog or vegetated/ocean surfaces, respectively [23,25]. However, the IR-based sea fog detection algorithm is limited under twilight conditions. Recently, a sea fog detection algorithm based on the decision tree approach was presented [26]. Wan et al. [27] presented a sea fog detection algorithm based on dynamic thresholds at dawn and dusk for the Yellow Sea and Bohai Sea using many bands (0.47, 0.64, 0.86, 1.6, 3.9, and 11.2 μm) of the AHI data.

In this study, we present a novel daytime sea fog detection algorithm with the advantage of the VIS band and compensating for the disadvantages of the IR-based algorithm in twilight conditions around the Yellow Sea region using observations from the AHI [8]. First, we define the study area within the Yellow Sea and the AHI data. Second, the developed method to detect sea fog based on the Normalized Difference Snow Index (NDSI) is described in detail. Third, the findings of several case studies on sea fog or mixtures of sea fog and clouds performed using the proposed algorithm are compared to the results of sea fog detection based on the SWIR band and BTD method to demonstrate the algorithm's efficiency, especially under twilight conditions. Fourth, the advantages and disadvantages of the proposed algorithm are discussed. Finally, the summary and conclusion of this study are described.

2. Study Area and Data

In this study, we chose the Yellow Sea surrounded by the Korean Peninsula and parts of China as the study area because of the area's frequent sea fog occurrence rate. Figure 1 shows the study area with an occurrence of sea and land fog on 14 March 2018, at 00:30 UTC (09:30 Korean Standard Time (KST)) observed from the AHI.

A large distribution of sea fog can easily be observed in the Yellow Sea, while instances of land fog occur in the coastal and inland areas of the Korean Peninsula and China. This study, however, focuses on the sea fog. Thus, land fog was masked using the land/sea flag information included by the AHI data.

Recently, advanced geostationary meteorological satellites with 16 spectral bands from VIS to IR, such as the Geostationary Operational Environmental Satellite (GOES)-16 [28], Himawari-8/9 [8], and GeoKompsat-2 Atmosphere (GK-2A) [29] have become operational. Specifically, Himawari-8/9 and GK-2A are appropriate for monitoring the sea fog in the Yellow Sea because they have widespread spatial coverage and a high temporal resolution. This study used Himawari-8 data equipped with an AHI sensor containing three VIS channels (0.47, 0.51, and 0.64 μm), three near-IR (NIR) channels (0.86, 1.61, and 2.26 μm), and 10 IR channels [8,25]. The spatial resolution at the nadir point is 0.5 km for the VIS channel at 0.64 μm, 1 km for the VIS channels at 0.47, 0.51, and 0.86 μm, and 2 km for the remaining NIR and all IR channels. The AHI can make full-disk measurements every 10 min, and observations of Japan and other target areas can be acquired every 2.5 min [8]. Table 1 summarizes the characteristics of the AHI sensor and their atmospheric applications.

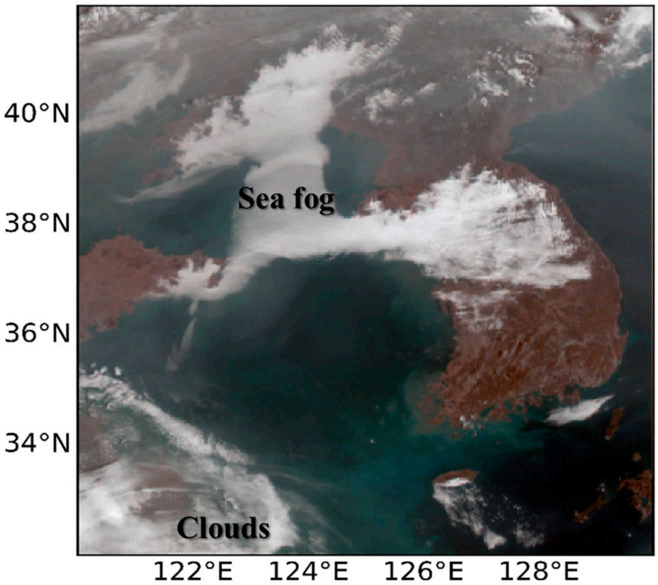

Figure 1. Study area of the Yellow Sea. The Red-Green-Blue (RGB) image observed from the Advanced Himawari Imager (AHI) sensor shows sea fog and clouds on 14 March 2018, 00:30 UTC (09:30 Korean Standard Time (KST)).

Table 1. Characteristics of the AHI channels.

Channel	Central Wavelength (μm)	Spatial Resolution (km)	Physical Properties
1	0.47	1	Vegetation, Aerosol
2	0.51	1	Vegetation, Aerosol
3	0.64	0.5	Low cloud, Fog
4	0.86	1	Vegetation, Aerosol
5	1.6	2	Cloud phase
6	2.3	2	Particle size
7	3.9	2	Low cloud, Fog, Forest fire
8	6.2	2	Mid- and upper-level moisture
9	6.9	2	Mid-level moisture
10	7.3	2	Mid- and lower-level moisture
11	8.6	2	Cloud phase, SO_2
12	9.6	2	Ozone content
13	10.4	2	Cloud imagery, Information of cloud top
14	11.2	2	Cloud imagery, Sea surface temperature
15	12.4	2	Cloud imagery, Sea surface temperature
16	13.3	2	Cloud top height, CO_2

We used the reflectance data of AHI green band (0.51 μm) and NIR band (1.6 μm) provided by the National Meteorological Satellite Centre (NMSC) of the Korea Meteorological Administration (KMA). Table 2 summarizes the case study of fog events evaluated in this study.

Table 2. Cases including sea fog used in this study.

Cases	Date	Purpose
Fogy and partly cloudy	11 March 2017. 00:30 UTC	test
	14 March 2018. 00:30 UTC	algorithm development
	24 February 2019. 02:00 UTC	test
	1 March 2019. 01:30 UTC	test
	26 March 2019. 02:00 UTC	test

Table 2. *Cont.*

Cases	Date	Purpose
Foggy and cloudy	9 April 2018. 04:00 UTC	test
	27 May 2018. 22:30 UTC	test
	6 June 2018. 00:30 UTC	test
	4 June 2019. 01:30 UTC	test
Weak signal of SWIR band	27 May 2018. 22:30 UTC	test
Absence of SWIR data	11 March 2017. 01:20 UTC	test
	30 April 2017. 22:30 UTC	test
	1 June 2017. 02:20 UTC	test
Continuous variation of sea fog with 30-min interval	13 March 2018. 22:30 UTC 14 March 2018. 03:00 UTC	test
	26 March 2018. 00:00–04:00 UTC	test

3. Method

3.1. NDSI and Reflectance

Sea fog and clouds show different roughness patterns in the visible bands [26]. Generally, the 0.51 µm band shows equal brightness levels for both clouds and snow cover. Thus, the homogeneity is useful for distinguishing sea fog from low water clouds [26], because the top of sea fog is relatively smooth, while cloud tops are rough due to motion fluctuation [30].

In addition, the 1.6 µm band is transparent for the atmosphere and not reflective for snow [10] as it benefits from the relatively large difference between the refraction components of water and ice. Thus, this SWIR band is useful to distinguish sea fog from ice clouds in satellite applications.

The NDSI is a combination of visible and SWIR bands. The NDSI can evaluate atmospheric effects and observing angle dependence [31]. Thus, it has been used in a previous snow cover study [32].

Therefore, this study proposes an algorithm to detect sea fog using a combination of the NDSI [33,34] and the reflectance in the AHI green band (0.51 µm) because of the advantage of the VIS band for distinguishing sea fog from low clouds and that of the SWIR band for separating sea fog from ice clouds.

The NDSI [34] was computed by dividing the difference in reflectance observed in the AHI green band (0.51µm) and the SWIR band (1.6 µm) as follows:

$$NDSI_{obs} = \frac{R_{0.51\mu m} - R_{1.6\mu m}}{R_{0.51\mu m} + R_{1.6\mu m}} \tag{1}$$

where $R_{0.51\mu m}$ and $R_{1.6\mu m}$ are the reflectances at 0.51 and 1.6 µm of the AHI, respectively.

Figure 2 shows an example of the signals for sea fog and sea surfaces from the $NDSI_{obs}$ at the same date and time with that shown in Figure 1. The $NDSI_{obs}$ values are low (0 to 0.4) for sea fog and medium (0.4 to 0.6) and high (0.6 to 0.8) for sea surfaces.

3.2. Regression Relationship Between NDSI and the VIS Green Band

To identify the spectral features of sea fog, we chose sea fog pixels separately from fog-free and cloud-free sea surfaces, as shown in Figure 3a, on March 14 2018, at 00:30 UTC (09:30 KST, daytime). Figure 3b shows the scatter-plot of distributions of sea fog and sea surface in NDSI versus reflectance at AHI 0.51 µm band ($R_{0.51\mu m}$) on the same date as Figure 3a. Sea fog pixels were distributed in a specific area within the NDSI-$R_{0.51\mu m}$ plane; this approach was different from other pixels such as sea surfaces because of the distinct optical properties among sea fog and sea surfaces in VIS bands. Distinctively, sea fog pixels were clustered in the NDSI-$R_{0.51\mu m}$ plane.

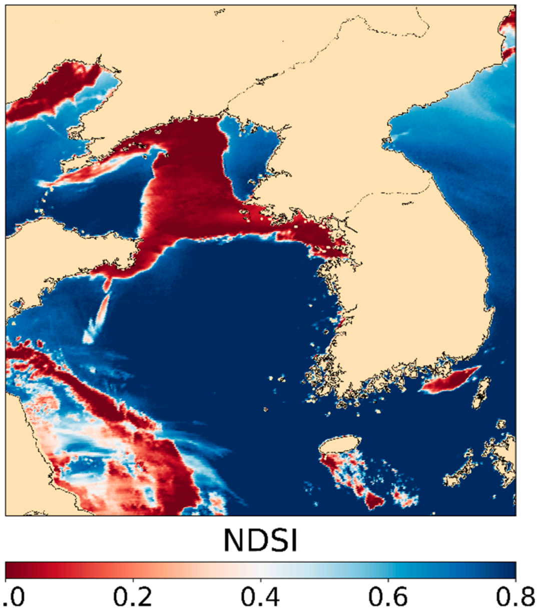

Figure 2. Example of $NDSI_{obs}$ on 14 March 2018, 00:30 UTC (09:30 Korean Standard Time (KST)).

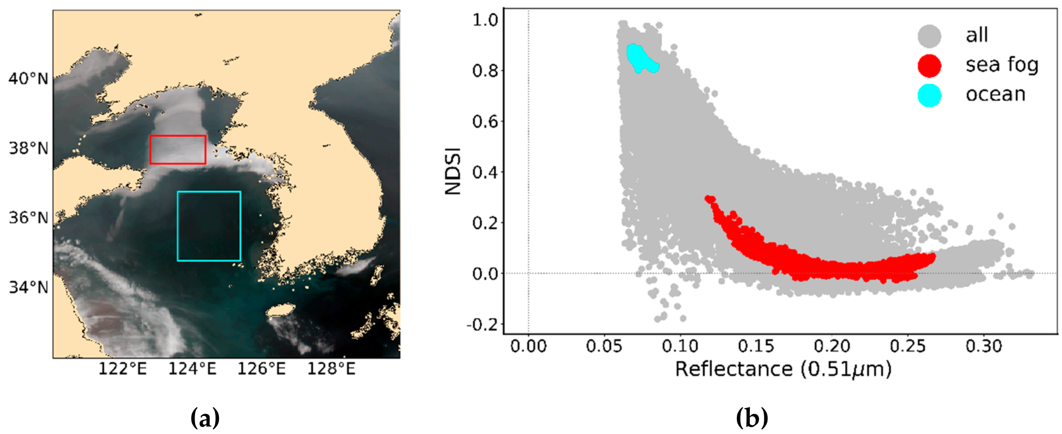

Figure 3. Case study examples. (**a**) AHI true-color images and (**b**) distributions of sea fog and sea surface pixels versus all pixels in the Yellow Sea in (**a**). The pixels in the land area were excluded.

To develop a sea fog detection algorithm, we chose the 0.51 µm band as an independent parameter to map the NDSI value. Our algorithm was constructed as follows.

First, we proposed the following regression relationship between NDSI and $R_{0.51\mu m}$ as follows.

$$NDSI_{cal} = a_0 + a_1 \cdot R_{0.51\mu m} + a_2 \cdot R^2_{0.51\mu m} \quad (2)$$

where $NDSI_{cal}$ is the calculated NDSI using $R_{0.51\mu m}$ as an independent variable, $R_{0.51\mu m}$ is the reflectance at band 2 (0.51 µm) of the AHI, and a_0, a_1, and a_2 are the regression coefficients for sea fog detection. For the case shown in Figure 3b, the regression coefficients a_0, a_1, and a_2 of $NDSI_{cal}$ were 1.100, −10.161, and 23.544, respectively.

Second, we realized that uncertainties may occur in the NDSI values using Equations (1) and (2). Thus, we considered the uncertainty of fog detection using a range of threshold value (σ) for sea fog pixels around the regression relationships, which was estimated from the distribution of NDSI difference ($NDSI_{diff}$) between observations ($NDSI_{obs}$) and calculations ($NDSI_{cal}$) as follows:

$$NDSI_{obs} - NDSI_{cal} < \sigma \quad \text{for sea fog detection} \tag{3}$$

where σ is the threshold value to be determined from the case studies, which was the maximum value of the $NDSI_{diff}$ in the manually-chosen sea fog pixels.

Figure 4a displays the area chosen for sea fog (red box), clouds (green box), and fog-free and cloud-free sea surfaces (blue box) based on the $NDSI_{obs}$ in Figure 2. Figure 4b shows the scatter-plot of distributions of sea fog, clouds, and sea surface in $NDSI_{obs}$ versus $NDSI_{diff}$ on the same date as Figure 4a. The red, cyan, and blue dots indicate the pixels of sea fog, clouds, and clear-sky sea surface, respectively. The grey dots indicate all pixels in the Yellow Sea excluding land surface. The land pixels were masked using the land/sea mask information. Sea fog pixels were distributed in a specific area within the $NDSI_{diff}$-$NDSI_{obs}$ plane. The $NDSI_{obs}$ was not enough to distinguish sea fog from clouds, while $NDSI_{diff}$ was sufficient. Distinctively, sea fog pixels were separable from cloud pixels in the $NDSI_{diff}$-$NDSI_{obs}$ plane. Sea fog and clear-sky sea surface pixels were distinctly clustered in the $NDSI_{obs}$ and $NDSI_{diff}$ plane. From this case, the $NDSI_{obs}$ and $NDSI_{diff}$ for sea fog determination ranged from −0.029 to 0.29, and −0.065 to 0.076, respectively. Thus, the threshold value (σ) of the $NDSI_{diff}$ was determined to be 0.076 for sea fog detection.

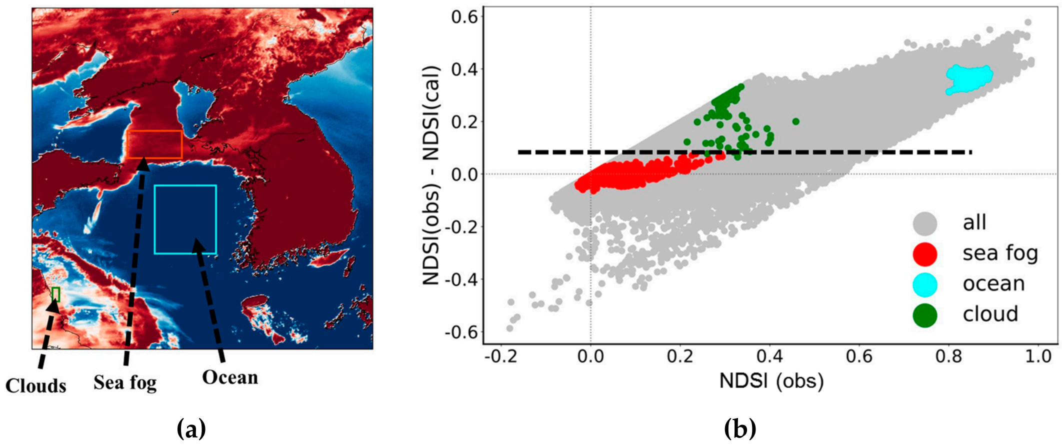

Figure 4. (**a**) Area selection of sea fog, clouds, and sea surface in the $NDSI_{obs}$ data. (**b**) Distributions of sea fog, clouds, sea surface pixels, and all pixels in the Yellow Sea in the $NDSI_{diff}$-$NDSI_{obs}$ plane.

3.3. Sea Fog Detection Using 3.9 µm of AHI

A SWIR band has the capability of detecting low-level cloud and fog [8]. The 3.9 µm SWIR band is traditionally used for fog detection because of its sensitivity to the thermal energy. Physically, sea fog and clouds have different brightness temperatures at the 3.9 µm band because of the altitude difference between sea fogs and clouds. The split window algorithm (SWA) has widely been used for the analysis and classification of satellite imagery [35]. The BTD between the 11 and 3.7 µm bands (BTD11-3.7) are effective for detecting low-level water clouds during the daytime [35,36]. In addition, the BTD between the 11 and 3.7 µm bands with the geostationary satellite is effective for nighttime fog detection across a wide range of terrain and temperature regimes if fog is not obscured by any clouds above [24]. However, this BTD method is limited in shallow fog detection because of small BTD values within the range of instrument noise [26,37]. In addition, the 3.9µm band for daytime fog detection has an unstable threshold affected by solar and Earth radiation [37].

In this study, the proposed sea fog detection algorithm was compared with the sea fog determined by the BTD methods between the 11.2 and 3.9 µm bands of the AHI for various case studies. This approach was taken because of the lack of ground-based sea fog observation data. The threshold values of sea fog using BTD was determined by using Otsu's method, which extracts objects from their background using binarization for the distribution of the histogram [38,39]. Notably, for algorithm validation, this study did not use the data of locations and types of clouds and aerosols provided by the Cloud-Aerosol Lidar with Orthogonal Polarization (CALIOP) instrument on board the CALIPSO satellite [40] because of its low spatial and temporal coverage. In addition, this study did not apply any cloud mask information to develop the sea fog detection algorithm.

Figure 5 shows an example of the brightness temperatures at AHI 3.9 µm and the BTD between AHI 3.9 µm and AHI 11.2 µm, which included sea fog, clouds, and a clear-sky sea surface in the study area. We can distinguish the sea fog area (dark grey color) from clouds (white color pixels) in Figure 5a, from that (grey color) in Figure 5b. Figure 5c displays the results of the Otsu method with the threshold value and histogram of the BTD between AHI 3.9 µm and AHI 11.2 µm. Figure 5d shows the final sea fog area result determined after applying the threshold value to the AHI data.

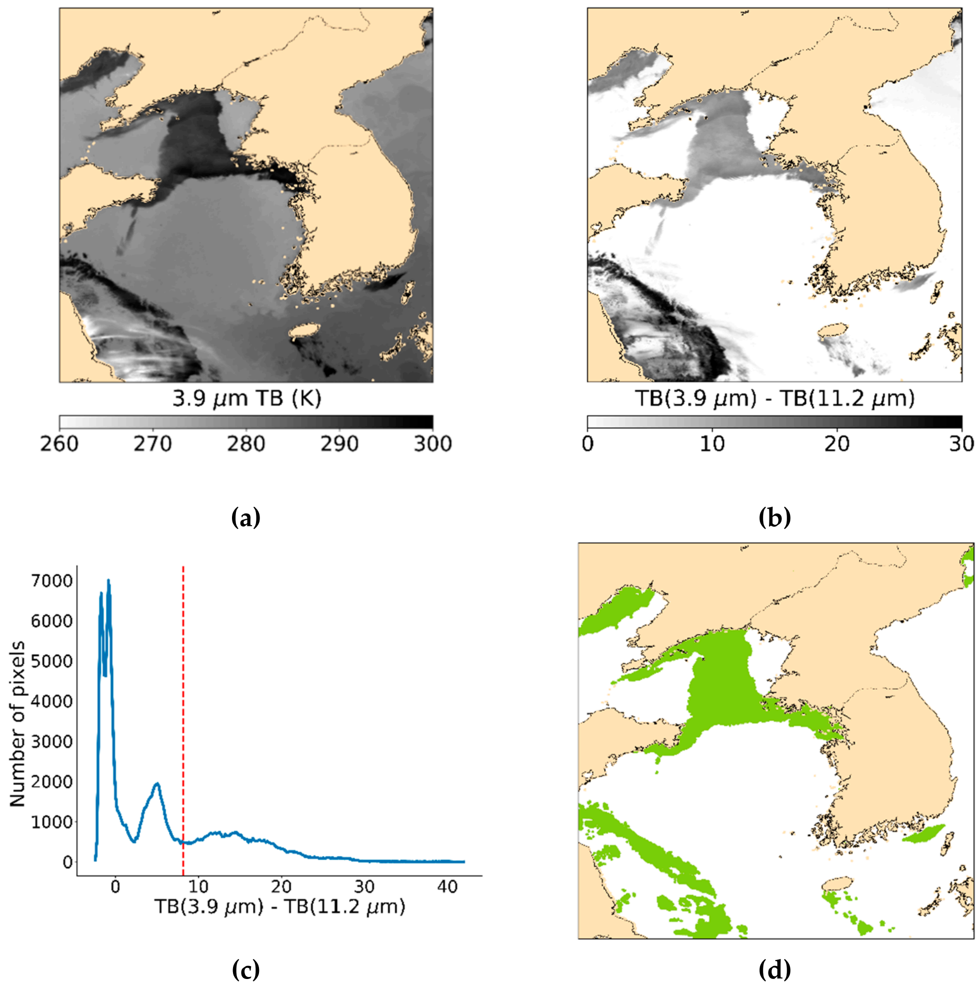

Figure 5. Examples of (**a**) brightness temperature (TB) at AHI 3.9 µm and (**b**) brightness temperature differences (BTD) between AHI 3.9 µm and AHI 11.2 µm, (**c**) histogram of BTD and threshold value determined using the Otsu method, and (**d**) the sea fog area after applying the threshold value.

3.4. Statistical Comparison

In this study, the pixel-by-pixel statistical comparison between the proposed sea fog detection algorithm with NDSI and the 0.51 µm band and the sea fog data obtained from BTD using the 3.9 µm and 11.2 µm bands of AHI was performed using the probability of detection (POD), post agreement (PAG), critical success index (CSI), and Heidke skill score (HSS) metrics as follows:

$$POD = \frac{a}{a+c} \quad (4)$$

$$PAG = \frac{a}{a+b} \quad (5)$$

$$CSI = \frac{a}{a+b+c} \quad (6)$$

$$HSS = \frac{2(ad-bc)}{(a+c)(c+d)+(a+b)(b+d)} \quad (7)$$

where a means that both the proposed sea fog and the BTD sea fog indicate a sea fog pixel, b means that the proposed algorithm shows a sea fog pixel while BTD does not show a sea fog pixel, c means that the proposed algorithm does not indicate a sea fog pixel while BTD shows a sea fog pixel, and d means that both algorithms do not show sea fog (Table 3). The statistical results between the proposed sea fog detection algorithm and the BTD sea fog algorithm are considered in accordance if the POD, PAG, CSI, and HSS are close to 1 [41]. The contingency table is summarized in Table 3.

Table 3. Contingency table.

	BTD = 1 (Yes)	**BTD = 0 (No)**
Proposed algorithm = 1 (Yes)	a	b
Proposed algorithm = 0 (No)	c	d

Figure 6 shows a flow chart of the proposed fog detection algorithm. First, the AHI calibrated reflectances at 0.51 and 1.6 μm were used as input data. Next, the NDSI was calculated. Notably, any cloud flag information was not provided and applied. Sea fog pixels were retrieved using the proposed sea fog detection algorithm using the NDSI and $NDSI_{diff}$. Finally, our sea fog detection algorithm was compared with the sea fog pixels retrieved using AHI 3.9 μm and the BTD between SWIR and LWIR via the Otsu method.

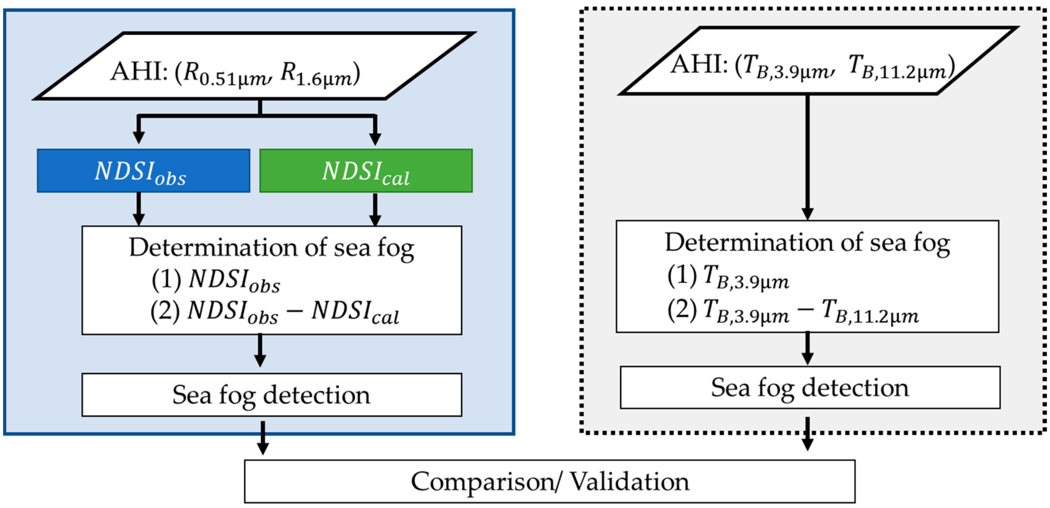

Figure 6. Flow chart of the proposed fog detection algorithm.

4. Results

4.1. Sea Fog Detection Algorithm

Figure 7 shows an example of sea fog detection results using the proposed sea fog detection algorithm on the same date as Figure 1. Notably, any cloud mask information was not applied. Figure 7a displays the difference between $NDSI_{obs}$ and $NDSI_{cal}$. The $NDSI_{obs} - NDSI_{cal}$ values of sea fog were relatively lower than those for sea surface and clouds. Figure 7b shows the sea fog area determined from the proposed algorithm in the NDSI-$R_{0.51\mu m}$ plane. The proposed sea fog detection algorithm produced qualitatively similar results to the sea fog using the AHI 3.9 µm and BTD between SWIR and LWIR via Otsu's method in Figure 5d.

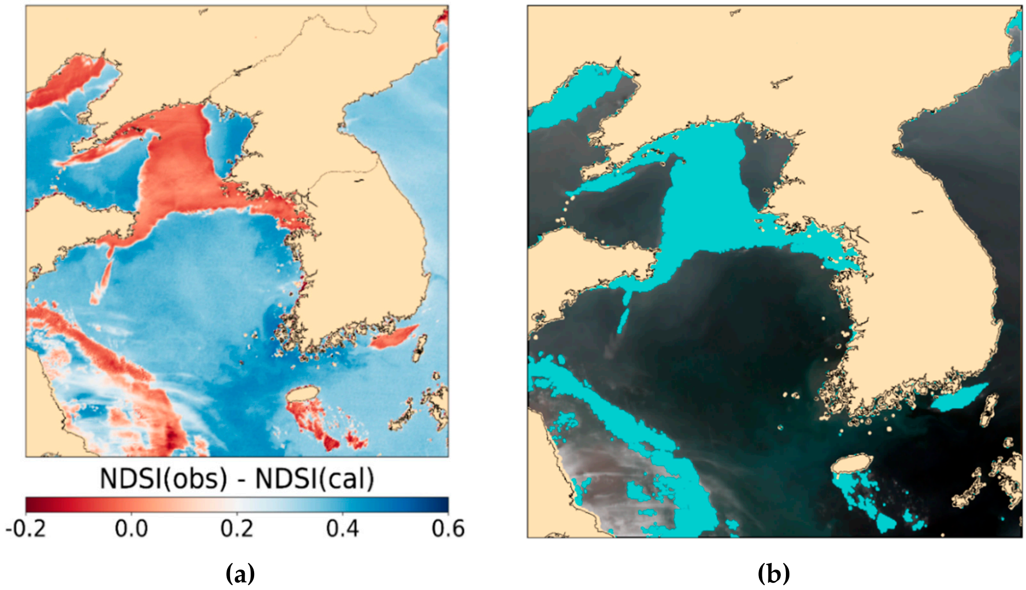

Figure 7. (**a**) $NDSI_{obs}$–$NDSI_{cal}$ and (**b**) results for sea fog detection using the proposed algorithm.

Figure 8 shows a qualitative comparison of the proposed sea fog detection algorithm and the AHI BTD sea fog in Figure 5. The purple color indicates that both sea fog algorithms detected pixels as sea fog. The cyan pixels mean that only the proposed sea fog algorithm detected the pixels as sea fog. The greenish pixels indicate that only the BTD sea fog algorithm detected the pixels as sea fog. A yellow color indicates the masked land area. In this case, POD, PAG, CSI, and HSS were 0.954, 0.887, 0.851, and 0.911, respectively.

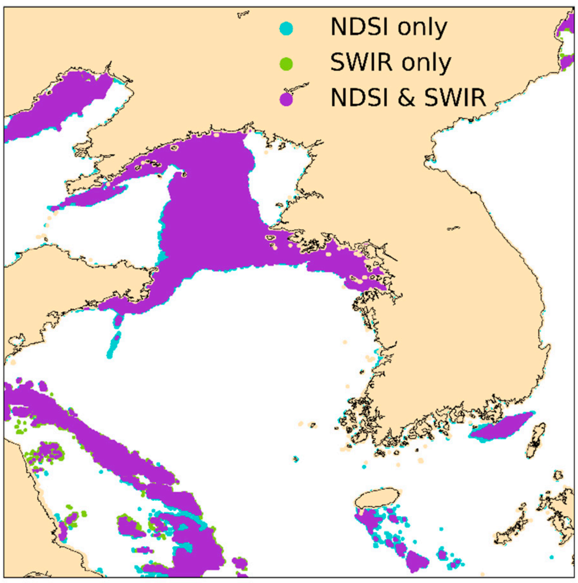

Figure 8. Quantitative comparison of the proposed sea fog detection algorithm and AHI BTD sea fog algorithm. POD, PAG, CSI, and HSS values were 0.954, 0.887, 0.851, and 0.911, respectively.

4.2. Foggy and Partly Cloudy Cases

Figure 9 shows the results of the proposed sea fog detection algorithm for foggy and partly cloudy weather cases. The first column shows the true color Red-Green-Blue (RGB) images. The second column shows the black and white images of AHI 3.9 µm. The third column shows the sea fog area of the proposed sea fog detection algorithm. The fourth column displays the comparison results of sea fog detection between the BTD algorithm and the proposed algorithm for sea fog cases on 24 February 2019, at 02:00 UTC, 1 March 2019, at 01:30 UTC, and 26 March 2019, at 02:00 UTC. The POD ranged from 0.843 to 0.981. The PAG ranged from 0.742 to 0.935. The CSI ranged from 0.731 to 0.874. The HSS ranged from 0.835 to 0.927. Thus, the two algorithms were mostly in accordance with each other. Table 4 summarizes the POD, PAG, CSI, and HSS values for each case.

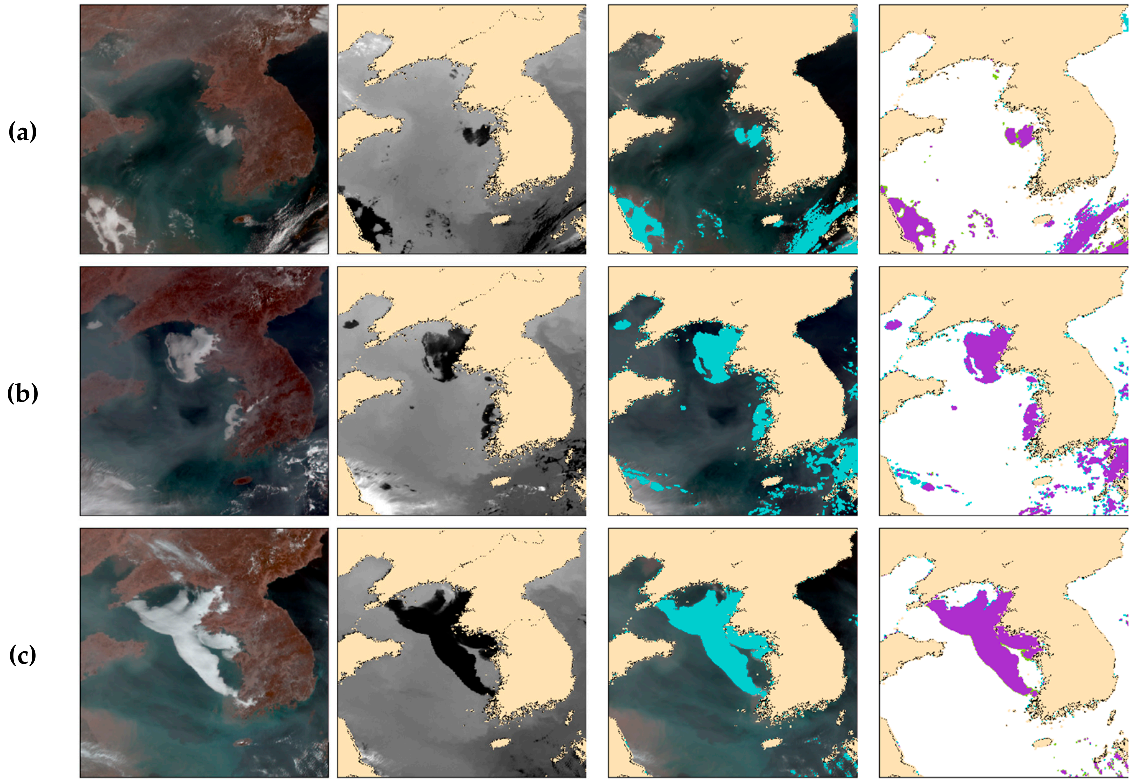

Figure 9. Results of the proposed sea fog detection algorithm for foggy and partly cloudy weather cases on (**a**) 24 February 2019, at 02:00 UTC, (**b**) 1 March 2019, at 01:30 UTC, and (**c**) 26 March 2019, at 02:00 UTC. The green and cyan colors indicate the sea fog pixels obtained using only AHI 3.9 µm and the BTD algorithm and only the proposed sea fog algorithm, respectively. The purple color indicates that both sea fog algorithms detected pixels as sea fog.

Table 4. Statistical results for foggy and partly cloudy cases.

	POD	PAG	CSI	HSS
24 February 2019 02:00 UTC	0.843	0.886	0.760	0.857
1 March 2019 01:30 UTC	0.981	0.742	0.731	0.835
26 March 2019 02:00 UTC	0.930	0.935	0.874	0.927

4.3. Foggy and Cloudy Cases

Figure 10 shows the results of the proposed sea fog detection algorithm for a mixture of fog and clouds. Notably, the proposed algorithm is still in accordance with the BTD sea fog detection algorithm. However, both the proposed sea fog detection algorithm and the BTD sea fog detection algorithm misidentified sea fog as clouds when the sea fog occurred under clouds. Thus, the POD, PAG, CSI, and HSS values were worse in foggy and cloudy cases than in foggy and partly cloudy cases. However, the range of the statistical scores were reasonable. POD ranged from 0.684 to 0.898, PAG ranged from 0.633 to 0.984, CSI ranged from 0.590 to 0.711, and HSS ranged from 0.688 to 0.790. Table 5 summarizes the POD, PAG, CSI, and HSS for each case.

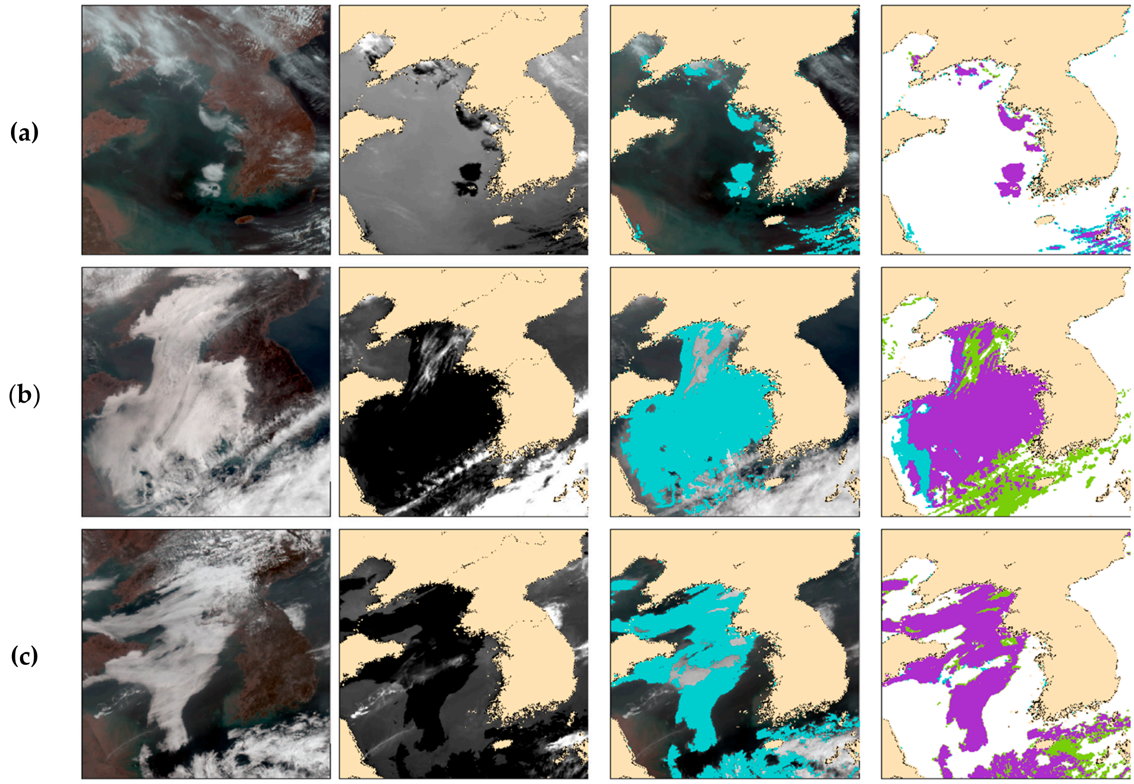

Figure 10. Sea fog and cloud mixtures. Results of the proposed sea fog detection algorithm on (**a**) 9 April 2018, at 04:00 UTC, (**b**) 6 June 2018, at 00:30 UTC, and (**c**) 4 June 2019, at 01:30 UTC. The green and cyan colors indicate the sea fog pixels obtained using only AHI 3.9 μm and the BTD algorithm and only the proposed sea fog algorithm, respectively. The purple color indicates that both sea fog algorithms detected pixels as sea fog.

Table 5. Statistical results for sea fog and cloud mixtures.

	POD	PAG	CSI	HSS
9 April 2018 04:00 UTC	0.898	0.633	0.590	0.734
6 June 2018 00:30 UTC	0.684	0.872	0.621	0.688
4 June 2019 01:30 UTC	0.719	0.984	0.711	0.790

4.4. Cases of Sea Fog Variation with 30-Minute Intervals

Figure 11 shows the results of the proposed sea fog detection algorithm for continuous variation of sea fog on 26 March 2019, from 00:00 UTC to 04:00 UTC with 30-min intervals. The first, second, third, and fourth rows indicate the AHI RGB, the brightness temperature at 3.9 μm, $NDSI_{obs} - NDSI_{cal}$, and sea fog detection results using the proposed algorithm, respectively. The fifth row shows the temporal variation of the statistical comparison between the two sea fog algorithms. This case shows the stable accordance between the two sea fog detection algorithms.

Time	00:00	00:30	01:00	01:30	02:00	02:30	03:00	03:30	04:00

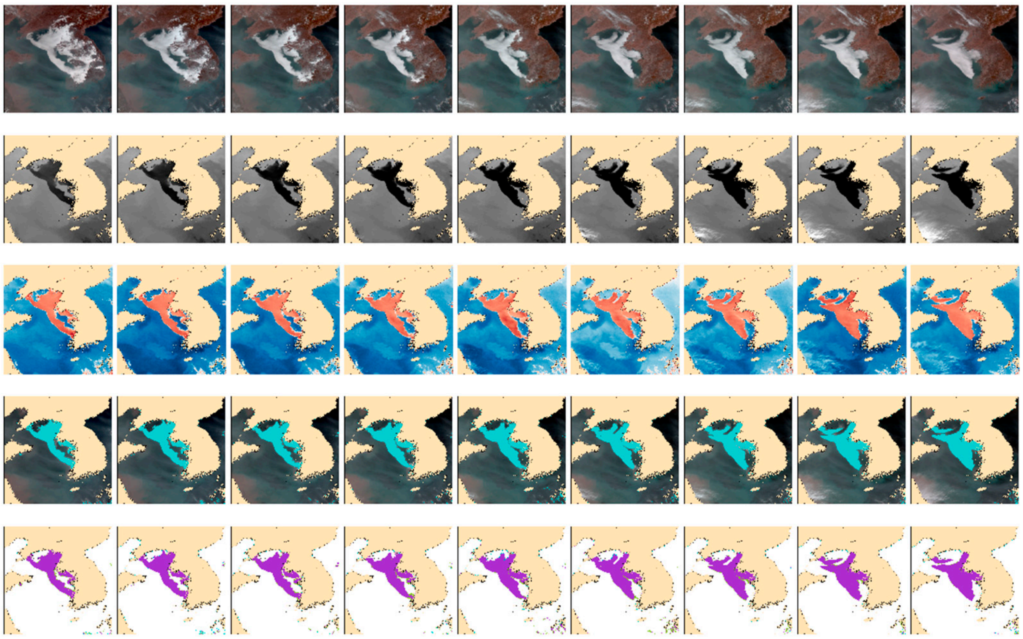

POD	0.909	0.972	0.927	0.914	0.930	0.923	0.912	0.942	0.969
PAG	0.970	0.941	0.948	0.946	0.935	0.964	0.954	0.962	0.947
CSI	0.884	0.916	0.882	0.868	0.874	0.893	0.873	0.908	0.919
HSS	0.934	0.953	0.933	0.924	0.927	0.939	0.927	0.948	0.954

Figure 11. Temporal variation of sea fog on 26 March 2019, from 00:00 UTC to 04:00 UTC with 30-min intervals in an RGB image, the brightness temperature at 3.9 µm, $NDSI_{diff}$ results for sea fog detection, and the statistical comparison between two sea fog algorithms.

5. Discussion

5.1. Advantage of the Proposed Algorithm

In this section, we present the advantage of the proposed sea fog detection algorithm. As stated previously, the BTD method based on IR observations cannot easily detect shallow fog because of small BTD values within the range of instrument noise [26,37] and the unstable thresholds [37]. The SWIR-based sea fog detection algorithm is limited in the twilight conditions. Thus, the signal of sea fog from the SWIR band is weak and cannot distinguish between sea fog and the sea surface because of the minimal differences in brightness temperatures between the sea fog and sea surface. Figure 12 shows an example where the proposed sea fog detection algorithm displays superior performance versus the BTD algorithm. In this case of near twilight, the difference in brightness temperature between the sea fog and sea surface is minimal. Thus, sea fog detection is difficult in this case. Meanwhile, the proposed sea fog algorithm detected sea fog in the Yellow Sea regardless of the existence of clouds. In this case, POD = 0.395, PAG = 0.256, CSI = 0.184, and HSS = 0.175.

Figure 13 shows the results of another continuous variation of sea fog on 13 March 2019, at 22:30 UTC to 14 March 2019, at 03:00 UTC with 30-min intervals. Notably, the brightness temperature at 3.9 µm increased over time. Specifically, the difference between sea fog and the sea surface was indistinguishable in twilight conditions (red box), such as on 13 March 2019, at 22:30 UTC. However, the proposed algorithm detects sea fog (red box) in the Yellow Sea. The performance of the 3.9 µm band improved over time within the algorithm. Thus, this example shows the applicability of using the proposed algorithm during twilight conditions.

5.2. Cases of Absence of Observation at SWIR Band

Figure 14 shows the results of the proposed sea fog detection algorithm for cases of no data from the 3.9 µm observation on 11 March 2017, at 01:20 UTC, 30 April 2017, at 22:30 UTC, and 1 June 2017, at 02:20 UTC. Thus, the proposed algorithm played a role in detecting sea fog when the brightness temperature at 3.9 µm was not available. The proposed algorithm still shows a qualitatively strong performance for foggy and partly cloudy conditions as well as mixed conditions of fog and clouds. These cases were not quantitatively compared because of a lack of 3.9 µm data.

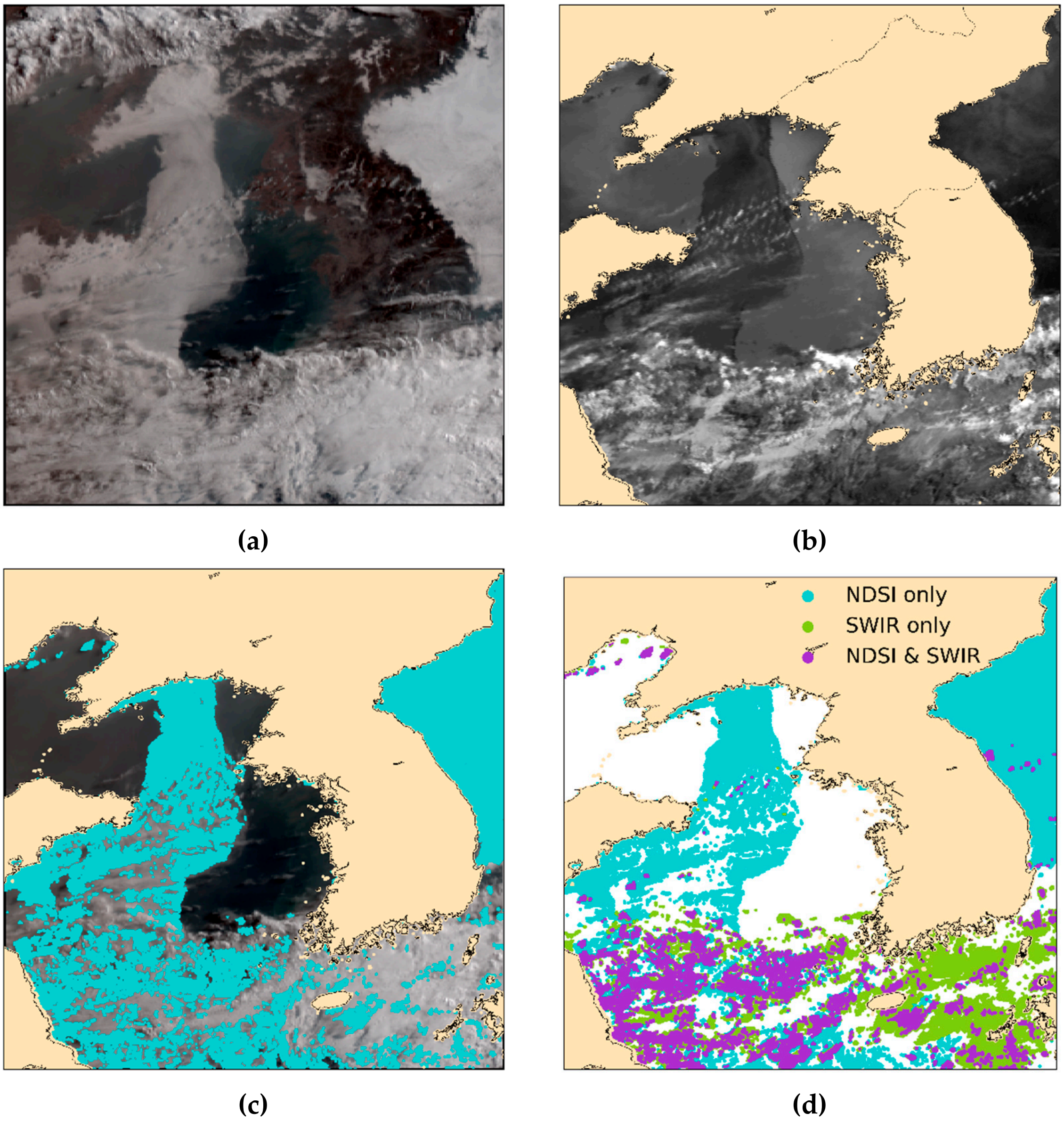

Figure 12. Case of sea fog in the twilight condition (27 May 2018, at 22:30 UTC) in (**a**) RGB image, (**b**) the brightness temperature at AHI 3.9 µm, (**c**) the proposed sea fog algorithm, and (**d**) the results of two sea fog algorithms.

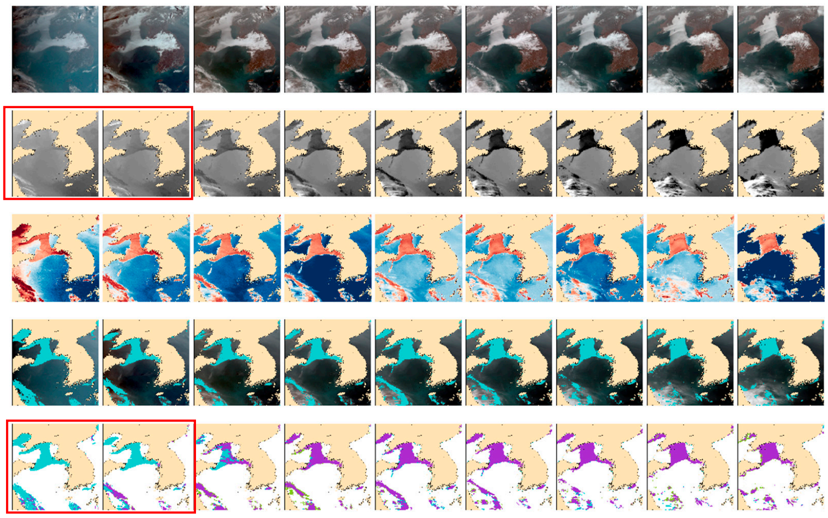

Time	22:30	23:00	23:30	00:00	00:30	01:00	01:30	02:30	03:00
POD	0.878	0.870	0.801	0.785	0.954	0.946	0.947	0.847	0.820
PAG	0.041	0.200	0.606	0.950	0.887	0.914	0.911	0.918	0.952
CSI	0.041	0.194	0.526	0.754	0.851	0.868	0.866	0.787	0.787
HSS	0.068	0.301	0.668	0.847	0.911	0.922	0.922	0.872	0.872

Figure 13. Temporal variation of sea fog on 13 March 2018, at 22:30 UTC to 14 March 2019, at 03:00 UTC with 30-min intervals in an RGB image, the brightness temperature at 3.9 μm, $NDSI_{obs} - NDSI_{cal}$, results for sea fog detection, and the statistical comparison between two sea fog algorithms.

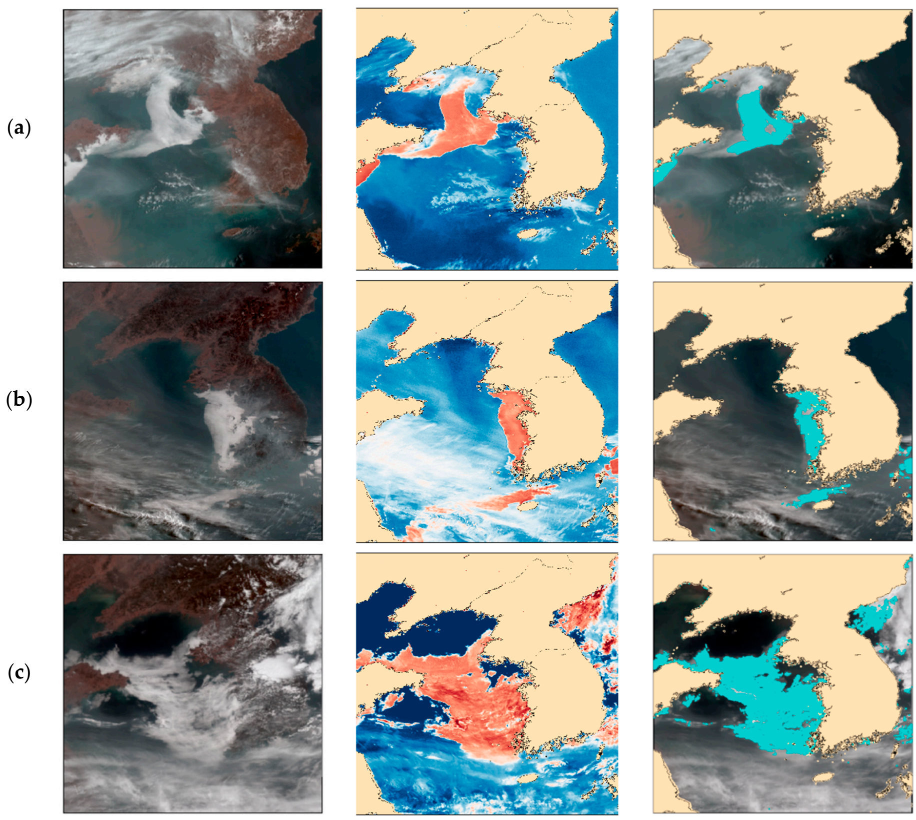

Figure 14. Cases of absence of SWIR band observation. Results for sea fog detection using the proposed algorithm on (**a**) 11 March 2017 at 01:20 UTC, (**b**) 30 April 2017, at 22:30 UTC, and (**c**) 1 June 2017, at 02:20 UTC.

6. Summary and Concluding Remarks

Low visibility due to fog often causes losses of life and socioeconomic activities throughout the Yellow Sea and its coastal regions. Cloud mask information is an important parameter retrieved from satellites for generating useful geophysical and meteorological parameters for surface information such as fog, surface temperature, vegetation, and so on. Discriminating between low clouds and fog using satellite observations has been difficult because of the radiometric similarity between them. This study presented a novel approach to detect sea fog using the observed reflectance at one VIS and one NIR bands of the AHI. Methodologically, we present the regression-based relationships between NDSI and reflectances at the green band of AHI for sea fog. The uncertainty caused by the regression relationships was considered with the threshold values estimated from a satellite-observed NDSI and a comparison between the satellite-observed NDSI and calculated NDSI. In this study, we did not use any cloud mask information. The results of our study show reasonable and high POD, PAG, CSI, and HSS values for various sea fog cases. Consequently, the proposed sea fog detection algorithm is useful for many users and a variety of optical satellites without SWIR bands such as 3.9 μm. In addition, our study is expandable to other geostationary satellites with spectral bands similar to those on the Himawari satellite, such as GOES-16/17 and Geo-Kompsat-2A. The combination of geostationary satellites can increase the temporal resolution of sea fog detection.

Author Contributions: Conceptualization, S.H.; methodology, H.-S.R. and S.H.; software, H.-S.R.; validation, H.-S.R. and S.H.; formal analysis, H.-S.R. and S.H.; investigation, H.-S.R. and S.H.; resources, S.H.; data curation, H.-S.R. and S.H.; writing—original draft preparation, H.-S.R.; writing—review and editing, S.H.; visualization, H.-S.R.; supervision, S.H.; project administration, S.H.; funding acquisition, S.H. All authors have read and agreed to the published version of the manuscript.

Funding: This research was funded by the Korea Meteorological Administration Research and Development Program under Grant KMI2020-00510 and supported by the "Technology development for Practical Applications of Multi-Satellite data to maritime issues" funded by the Ministry of Ocean and Fisheries, the Republic of Korea.

Acknowledgments: The authors thank anonymous reviewers for constructive and helpful comments on the manuscript.

Conflicts of Interest: The authors declare no conflicts of interest.

References

1. Zhang, S.; Li, M.; Meng, X.; Fu, G.; Ren, Z.; Gao, S. A comparison study between spring and summer fogs in the Yellow Sea-observations and mechanisms. *Pure Appl. Geophys.* **2011**, *169*, 1–17.
2. Zhang, S.; Xie, S.; Liu, Q.; Yang, Y.; Wang, X.; Ren, Z. Seasonal variations of Yellow Sea fog: Observations and mechanisms. *J. Clim.* **2009**, *22*, 6758–6772.
3. Wang, B.H. *Sea Fog*; Ocean Press: Beijing, China, 1985.
4. Heo, K.-Y.; Park, S.; Ha, K.-J.; Shim, J.-S. Algorithm for sea fog monitoring with the use of information technologies. *Meteorol. Appl.* **2014**, *21*, 350–359.
5. Lee, Y.-H.; Lee, J.-S.; Park, S.-K.; Chang, D.-E.; Lee, H.-S. Temporal and spatial characteristics of fog occurrence over the Korean Peninsula. *J. Geophys. Res.* **2010**, *115*, D14117.
6. Andrews, H.I.; Bright, J.M. Bright. evaluating fog detection using Himawari-8 satellite imagery and bispectral image processing. In Proceedings of the Asia-Pacific Solar Research Conference (APSRC), Sydney, Australia, 4–6 December 2018.
7. Letu, H.; Ishimoto, H.; Riedi, J.; Nakajima, T.Y.; Labonnote, L.C.; Baran, A.J.; Nagao, T.M.; Sekiguchi, M. Investigation of ice particle habits to be used for ice cloud remote sensing for the GCOM-C satellite mission. *Atmos. Chem. Phys.* **2016**, *16*, 12287–12303.
8. Bessho, K.; Date, K.; Hayashi, M.; Ikeda, A.; Imai, T.; Inoue, H.; Kumagai, Y.; Miyakawa, T.; Murata, H.; Ohno, T.; et al. An introduction to Himawari-8/9—Japan's new-generation geostationary meteorological satellites. *J. Meteor. Soc. Jpn.* **2016**, *94*, 151–183.
9. Vermote, E.; Justice, C.; Csiszar, I. Early evaluation of the VIIRS calibration, cloud mask and surface reflectance Earth data records. *Remote Sens. Environ.* **2014**, *148*, 134–145.

10. Shang, H.; Chen, L.; Letu, H.; Zhao, M.; Li, S.; Bao, S. Development of a daytime cloud and haze detection algorithm for Himawari-8 satellite measurements over central and eastern China. *J. Geophys. Res.* **2017**, *122*, 3528–3543.
11. Zhang, Z.; Platnick, S. An assessment of differences between cloud effective particle radius retrievals for marine water clouds from three MODIS spectral bands. *J. Geophys. Res.* **2011**, *116*, D20215.
12. Lai, R.; Teng, S.; Yi, B.; Letu, H.; Min, M.; Tang, S.; Liu, C. Comparison of cloud properties from Himawari-8 and FengYun-4A geostationary satellite radiometers with MODIS cloud retrievals. *Remote Sens.* **2019**, *11*, 1703.
13. Zhu, Z.; Woodcock, C.E. Automated cloud, cloud shadow, and snow detection in multitemporal Landsat data: An algorithm designed specifically for monitoring land cover change. *Remote Sens. Environ.* **2014**, *152*, 217–234.
14. Amato, U.; Antomadis, A.; Cuomo, V.; Cutillo, L.; Franzese, M.; Murino, L.; Serio, C. Statistical cloud detection from SEVIRI multispectral images. *Remote Sens. Environ.* **2008**, *112*, 750–766.
15. Hutchison, K.D.; Jackson, J.M. Cloud detection over desert regions using the 412 nanometer MODIS channel. *Geophys. Res. Lett.* **2003**, *30*, 2187.
16. Nakajima, T.Y.; Tsuchiya, T.; Ishida, H.; Matsui, T.N.; Shimoda, H. Cloud detection performance of spaceborne visible-to-infrared multispectral imagers. *Appl. Opt.* **2011**, *50*, 2601–2616.
17. Hutchison, K.D.; Iisager, B.D.; Hauss, B. The use of global synthetic data for pre-launch tuning of the VIIRS cloud mask algorithm. *Int. J. Remote Sens.* **2012**, *33*, 1400–1423.
18. Goodman, A.H.; Henderson-Sellers, A. Cloud detection and analysis: A review of recent progress. *Atmos. Res.* **1988**, *21*, 203–228.
19. Gaurav, S.; Jindal, P. Radiative transfer model simulations to determine the night time fog detection threshold. *ISPRS Arch.* **2018**, *XLII-5*, 511–517.
20. Jianhua, W.; Jing, S.; Shanwei, L.; Hui, S. The research on the spectral characteristics of sea fog based on CALIOP and MODIS data. *ISPRS Arch.* **2018**, *XLII-3*, 667–1671.
21. Ahn, M.; Sohn, E.; Hwang, B. A new algorithm for sea fog/stratus detection using GMS-5 IR data. *Adv. Atmos. Sci.* **2003**, *20*, 899–913.
22. Hunt, G. Radiative properties of terrestrial clouds at visible and infrared thermal window wavelengths. *Q. J. R. Meteorol. Soc.* **1973**, *99*, 346–369.
23. Eyre, J.; Brownscombe, J.; Allam, R. Detection of fog at night using Advanced Resolution Radiometer (AVHRR) imagery. *Meteorol. Mag.* **1984**, *113*, 266–271.
24. Ellrod, G. Advances in the detection and analysis of fog at night using GOES multispectral infrared Imagery. *Weather Forecast.* **1995**, *10*, 606–619. [CrossRef]
25. Zhuge, X.-Y.; Zou, X.; Wang, Y. A fast cloud detection algorithm applicable to monitoring and nowcasting of daytime cloud systems. *IEEE Trans. Geosci. Remote Sens.* **2017**, *55*, 1–9. [CrossRef]
26. Kim, D.; Park, M.-S.; Park, Y.-J.; Kim, W. Geostationary Ocean Color Imager (GOCI) marine fog detection in combination with Himawari-8 based on the decision tree. *Remote Sens.* **2020**, *12*, 149. [CrossRef]
27. Wan, J.H.; Jiang, L.; Xiao, Y.F.; Sheng, H. Sea fog detection based on dynamic threshold algorithm at dawn and dusk time. *ISPRS Arch.* **2019**, *XLII-3*, 159–163. [CrossRef]
28. Schmit, T.J.; Gunshor, M.M.; Menzel, W.P.; Gurka, J.J.; Li, J.; Bachmeier, A.S. Introducing the next-generation advanced baseline imager on GOES-R. *Bull. Am. Meteorol. Soc.* **2005**, *86*, 1079–1096. [CrossRef]
29. National Meteorological Satellite Center (NMSC). Available online: http://nmsc.kma.go.kr (accessed on 23 July 2019).
30. Houze, R.A. *Cloud Dynamics*, 53rd ed.; Academic Press: San Diego, CA, USA, 1993; p. 137.
31. Salomonson, V.; Appel, I. Estimating fractional snow cover from MODIS using the normalized difference snow index. *Remote Sens. Environ.* **2004**, *89*, 351–360. [CrossRef]
32. Xiao, X.M.; Shen, Z.X.; Qin, X.G. Assessing the potential of vegetation sensor data for mapping snow and ice cover: A normalized difference snow and ice index. *Int. J. Remote Sens.* **2001**, *22*, 2479–2487. [CrossRef]
33. Hall, D.K.; Riggs, G.A.; Salomonson, V.V.; Barton, J.S.; Casey, K.L.; Chien, N.E.; DiGirolamo, A.G.; Klein, H.; Powell, W.; Tait, A.B. Algorithm Theoretical Basis Document (ATBD) for the MODIS Snow and Sea Ice-Mapping Algorithms. Available online: https://modis-snow-ice.gsfc.nasa.gov/?c=atbd (accessed on 23 July 2019).
34. Tong, J.; Velicogna, I. A comparison of AMSR-E/Aqua snow products with in situ observations and MODIS snow cover products in the Mackenzie river basin, Canada. *Remote Sens.* **2010**, *2*, 2313–2322. [CrossRef]

35. Purbantoro, B.; Aminuddin, J.; Manago, N.; Toyoshima, K.; Lagrosas, N.; Sumantyo, J.T.S.; Kuze, H. Comparison of cloud type classification with split window algorithm based on different infrared band combinations of Himawari-8 Satellite. *Adv. Remote Sens.* **2018**, *7*, 218–234. [CrossRef]
36. Ackerman, S.A.; Strabala, K.I.; Menzel, W.P.; Frey, R.A.; Moeller, C.C.; Gumley, L.E. Discriminating clear sky from clouds with MODIS. *J. Geophys. Res.* **1998**, *103*, 32141–32157. [CrossRef]
37. Cermak, J.; Bendix, J. A novel approach to fog/low stratus detection using Meteosat 8 data. *Atmos. Res.* **2008**, *87*, 279–292. [CrossRef]
38. Otsu, N. A threshold selection method from gray-level histogram. *IEEE Trans. Geosci. Remote Sens.* **1979**, *9*, 62–66. [CrossRef]
39. Ban, H.-J.; Kwon, Y.-J.; Shin, H.; Ryu, H.-S.; Hong, S. Flood monitoring using satellite-based RGB composite imagery and refractive index retrieval in visible and near-infrared bands. *Remote Sens.* **2017**, *9*, 313. [CrossRef]
40. Winker, D.M.; Pelon, J.; Coakley, J.A., Jr.; Ackerman, S.A.; Charlson, R.J.; Colarco, P.R.; Flamant, P.; Fu, Q.; Hoff, R.M.; Kittaka, C.; et al. The CALIPSO mission: A global 3D view of aerosols and clouds. *Bull. Am. Meteorol. Soc.* **2010**, *91*, 1211–1229. [CrossRef]
41. Wilks, D.S. *Statistical Methods in the Atmospheric Sciences*; Academic Press: Oxford, UK, 2011.